

FULL PAPER

Measurement and modelling of electrical resistivity by four-terminal method during flash sintering of 3YSZ

Michiyuki YOSHIDA^{1,2,†}, Simone FALCO^{2,3} and Richard I. TODD²¹Gifu University, Faculty of Engineering, 1–1 Yanagido, Gifu 501–1193, Japan²University of Oxford, Department of Materials, Parks Road, Oxford OX1 3PH, UK³University of Oxford, Department of Engineering Science, Parks Road, OX1 3PJ, UK

Flash sintering is a newly developed technique to quickly densify conductive ceramics in the presence of an electric field. At a critical combination of field and temperature, densification takes place in a few seconds. This paper investigates the electrical resistivity during flash sintering of 3YSZ by the four-terminal method in combination with numerical modelling of electrical heating and temperature distributions. Densification rates were similar to those observed previously in specimens rapidly heated by methods not involving direct electrical heating. Temperature gradients caused by heat loss from the surface and non-uniform electrical heating led to differential sintering, specimen distortion and non-uniform grain size. The four point measurements revealed significant contact resistance at the power supply electrodes and allowed accurate measurement of the resistivity under the high current conditions of flash sintering. The specimen resistivity was lower for a given temperature under high current conditions and this was attributed to electronic conduction. Concurrent sintering led to a progressive reduction of resistivity during heating causing an increase in the apparent activation energy for electrical conduction. When the effect of sintering on resistivity was accounted for, the onset conditions for the “flash event” were accurately predicted on the basis of thermal runaway.

©2018 The Ceramic Society of Japan. All rights reserved.

Key-words : Zirconia, Flash sintering, Electrical resistivity

[Received November 28, 2017; Accepted March 30, 2018]

1. Introduction

“Flash Sintering”, as an extremely fast sintering method, has attracted much interest since it was first reported by Cologna et al. in 2010.¹⁾ In their original report, a DC electric field is applied to a sample (3 mol.% Y₂O₃-stabilized ZrO₂–YSZ) while it is heated in a conventional furnace and at a certain furnace temperature the densification takes place in a few seconds. Flash sintering has now been demonstrated with a wide range of different ceramics, such as 8YSZ (an ionic conductor),²⁾ Co₂MnO₄ (an electronic conductor),^{3,4)} La_{0.6}Sr_{0.4}Co_{0.2}Fe_{0.8}O₃ (a mixed ionic electronic conductor),⁵⁾ SrTiO₃ (a dielectric oxide),⁶⁾ Al₂O₃,⁷⁾ SnO₂,⁸⁾ SiC,^{9,10)} and Y₂O₃.¹¹⁾

The mechanisms responsible for flash sintering remain open to question.^{12,13)} Raj et al.¹²⁾ have suggested that avalanches of Frenkel defects are responsible both for the surge of electrical power dissipation observed in flash sintering and for the mass transport. Others, have shown that the power surge can be explained satisfactorily as thermal runaway resulting from the negative temperature coefficient of resistivity of most ceramics^{14)–18)} whilst

comparison with the sintering of powder compacts rapidly heated without an electric field suggests that the high densification rate may be at least in part a consequence of the fast heating in flash sintering.^{19,20)}

Further progress requires a better understanding of the conditions during flash sintering. This is a complex and dynamic process with transient temperatures, temperature gradients and constantly changing specimen characteristics (electrical resistivity, thermal conductivity, emissivity, dimensions) as sintering removes porosity and densifies the specimen. The response of the electrical contacts adds a further complication. Some of these quantities, such as the temperature profile within the specimen, are difficult to measure directly during flash sintering but may be deduced indirectly using analytical or numerical modelling if sufficient fundamental information is available.

One area where more information is needed is the electrical response of the specimen during flash sintering. In previous investigations (e.g. 14), 15)) this has been described phenomenologically in terms of an inverse Arrhenius expression for the resistivity (or equivalently an Arrhenius expression for the conductivity). For dense ceramics under constant conditions, this has a firm physical basis for both semi-conducting and ionically conducting ceramics and has been used successfully to describe

[†] Corresponding author: M. Yoshida; E-mail: myoshida@gifu-u.ac.jp

the resistivity of 3YSZ,^{21),22)} the ceramic in the present investigation, under such conditions. In flash sintering, however, this is clearly an oversimplification in that the fit to the inverse Arrhenius expression over the whole flash sintering process must incorporate several factors in addition to the underlying low current conductivity mechanism. The most obvious complication is that the specimen begins as a powder compact but becomes a dense ceramic during flash sintering. This is expected to reduce the electrical resistivity as heating and sintering progress. The response at the electrodes, where there may be contact resistance, electrode potentials, polarization etc. should also be considered, but has not been measured to our knowledge. Finally, the enormous increase in current during the “flash event” may change the underlying mechanism of conduction and hence the equation describing it. It is noted that the high current, high temperature regime appropriate to flash sintering has hardly been studied, most previous work having concentrated on the high temperature low voltage/current regime appropriate to fuel cells, sensors etc. on the one hand or the low temperature, very high voltage conditions of dielectric breakdown on the other.

In this investigation, we evaluated the electrical resistivity during flash sintering of 3YSZ by the four-terminal method to enable the separation of the specimen resistivity from the electrode response. The sample temperature was estimated using the black-body radiation equation²³⁾ so that the underlying resistivity-temperature behavior could be investigated. Numerical modelling of the sintered specimens under steady state conditions was used to check that the geometry of the experiments could be expected to return the correct resistivity, both with low electrical loading and under the extreme conditions of the constant current part of the flash sintering cycle. The model was also used to investigate the validity of the black-body temperature and the possible explanations for the electrical properties measured. This allowed the characteristics of the electric conduction mechanism under flash sintering to be compared with those under conventional conditions.

2. Experimental procedure

The specimens in this work were made by slip casting. 3 mol % yttria-stabilized zirconia powder (TZ-3Y-E Tosoh, Shuanshi, Japan) was used as starting material. 3YSZ powder was added to distilled water to give a solid loading of 55 wt %. 2 wt % (relative to the solid) of Dispex A40 was added as dispersant. Subsequently, an ultrasonic probe was used to break up any agglomerates in the slurry. The prepared slurry was slip cast in bar shaped plastic molds on a porous gypsum base. The cross-section of the green bodies was 5.8 mm × 2.3 mm. All the specimens had holes separated by 15 mm for the connections to the power supply. These were produced by setting aluminium pins with 1.5 mm in diameter in the specimen during slip casting. The pins were removed before the specimens had completely dried. Platinum wires with 0.3 mm diameter and a spacing of 10 mm were set in the specimen for the

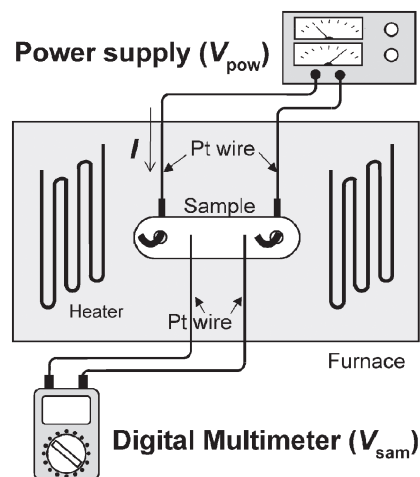


Fig. 1. Schematic illustration of the bar shaped sample geometry and the experimental set up for flash sintering.

measurement electrodes in the four-terminal measurements. The solidified green bodies were removed from the gypsum mold, and dried in an oven at 80°C for one day. The resulting green bodies were approximately 50% dense.

A schematic illustration of the experimental setup for flash sintering is shown in Fig. 1. The experiments were carried out in a modified box furnace that operates in ambient air. The original furnace door was replaced with an insulating refractory wall which had a quartz window in the middle to allow video recordings to be made of the specimens during flash sintering. The sample was suspended from the two wires by looping them over an alumina frame. The electrical field was applied with platinum electrodes. The connection between the electrodes and the specimen was made by inserting the electrodes through the holes in the specimens without the aid of conductive paint. This is the same as in the initial reports of flash sintering^{1),2)} and provides a “worst case” for the contact resistance. In this study, flash sintering was conducted at the isothermal furnace temperature of 900°C. Below 900°C no electric field was applied. Green samples were initially heated in the furnace at a rate of 7.5 °C/min to 600°C and then at 5 °C/min to 900°C, and held for 10 min to ensure uniform temperature. Subsequently, the electric field was applied in a stepwise fashion, in steps of 5–20 V until the flash event occurred at an applied field of ~100 V/cm. A commercial DC power source (360 V, 15 A, 1500 W, Elektro-Automatik, Viersen, Germany) was used and data were logged using Labview software. The voltage across the inner points for four terminal measurements was measured using a digital multimeter and accurate current measurements were made by measuring the voltage across a 10 Ω resistor in series with the circuit using another multimeter. The current limit at which the power supply switched from voltage control to current control was set to different levels for each specimen as explained in the results. Similar experiments were conducted on a dense, pre-sintered specimen and the green

body but under low electrical loading of 30 and 99 V/cm from the start of heating, respectively. These voltages were sufficiently low to avoid significant electrical heating and thermal runaway.

The flash sintered samples were cut at the embedded thinner Pt wires to obtain rectangular samples from the central part of the specimen. The relative density of these samples was measured by Archimedes' method with distilled water as the buoyant medium, taking 6.05 g/cm³ as the theoretical density of 3YSZ. The microstructure of the sintered samples was observed with a scanning electron microscope (Model S4800, Hitachi Co., Japan). The sintered bodies were sectioned along the central plane normal to the line connecting the electrodes, polished and thermally etched for 30 min at 1100°C, followed by the osmium coating. The grain size was defined as the equivalent circular diameter measured by the image analysis of SEM photographs.

3. Modelling

The modelling presented in this paper was performed with the commercial software COMSOL Multiphysics®.²⁴⁾ In particular, the AC/DC and the Heat transfer modules were used to simulate, respectively, the electrical and thermal behaviour of sintered 3YSZ, as well as their coupling.

Only the sintered specimens (both the pre-sintered, low voltage specimen and the flash sintered specimens in the constant current regime) were modelled. The experimentally measured dimensions of each specimen were used to generate steady state Finite Element (FE) models of each test, applying various boundary conditions, both in terms of electrode shape (e.g. half face, point source) and positions around the holes in the specimens. However, all the numerical results given explicitly in this paper refer to models with electrodes positioned at the top of the holes, as in the experimental setup (Fig. 1), and covering about 1/6 of the cylindrical surface.

The material was modelled as a perfect conductor with temperature-dependent conductivity and the simulations were used to find the equilibrium condition between the heat produced by Joule heating and the heat dissipated by radiation. The dependence of the conductivity of the material over the temperature has been expressed with an Arrhenius law:

$$\sigma = -\sigma_0 \exp\left(\frac{Q}{RT}\right) \quad (1)$$

where σ_0 and Q are equal to $6.45 \cdot 10^3 \Omega^{-1} \text{m}^{-1}$ and 76.06 kJ mol⁻¹, respectively. These are values calculated from the pre-sintered, low voltage specimen results in Section 4.5. The heat dissipation mechanism, instead, is described by the Stefan–Boltzmann law,²³⁾ which can be expressed as:

$$w_A = \sigma_S \varepsilon (T_s^4 - T_0^4) \quad (2)$$

where w_A is the dissipated power per unit area, σ_S is the Boltzmann constant, ε is the surface emissivity, and T_s and T_0 are, respectively, the surface and the ambient temper-

ature. The choice of the surface emissivity was based on the measurements of Tanaka et al.²⁵⁾ on sintered zirconia, and assumed to be equal to 0.7.

4. Experimental results

4.1 General features of flash sintering

Results for a typical isothermal experiment carried out with a maximum voltage of 135 V, the current limit set at 0.95 A, and the furnace temperature at 900°C, are shown in Fig. 2. The voltage and current shown in Fig. 2 are the “two terminal” values recorded by the power source. As reported by previous works,²³⁾ there were two well-defined regions once a critical voltage was applied: (1) a voltage control region, in which the current rises slowly at first and then more rapidly until it reaches a pre-programmed limit, followed by (2) a region with the power supply under current control, in which the voltage and the power dissipation reduce gradually to a steady state, in this case of ~60 V and 60 W respectively. The rapid increase in current at constant voltage shows that the specimen resistance was decreasing throughout the process, as shown in Fig. 2(c) so that the switch to current control results in a power spike [Fig. 2(d)]. These features demonstrate that the original results reported in the literature were successfully reproduced in this study.

4.2 Specimen temperature

The specimen temperature can rise considerably above the furnace temperature from Joule heating. The localization of heating along the line between the electrodes was also apparent in the experimental video recorded at higher current density after the switch to current control [Fig. 3(b)]. The brightness of the specimen was also higher towards the anode. The line of localization was above the center-line because the electrodes contacted the specimen at the topmost point of the holes as shown in Fig. 1.

The non-uniform temperature is discussed in section 5.1, but we first obtained an analytical estimate on the assumption of a uniform sample temperature, T_s , in the section between the inner “four terminal” wires for the constant current regime, from the black body radiation model based on the Stefan–Boltzmann law.²³⁾ According to this model, the specimen temperature at steady state can be derived from Eq. (2):

$$T_s = \left(T_0^4 + \frac{W}{A\varepsilon\sigma_S}\right)^{1/4} \quad (3)$$

where T_0 is the furnace temperature, W is the electrical power dissipated, A is the instantaneous surface area, ε is the emissivity and σ_S is Stefan–Boltzmann constant. The dimensions of the sintered specimens were used for A in this case; it should be noted that the shrinkage during sintering makes a significant difference to the calculated temperature (>100°C for some of the examples here). The choice of emissivity is particularly problematic as it can be expected to vary with density during sintering as well as with surface roughness, wavelength and temperature.

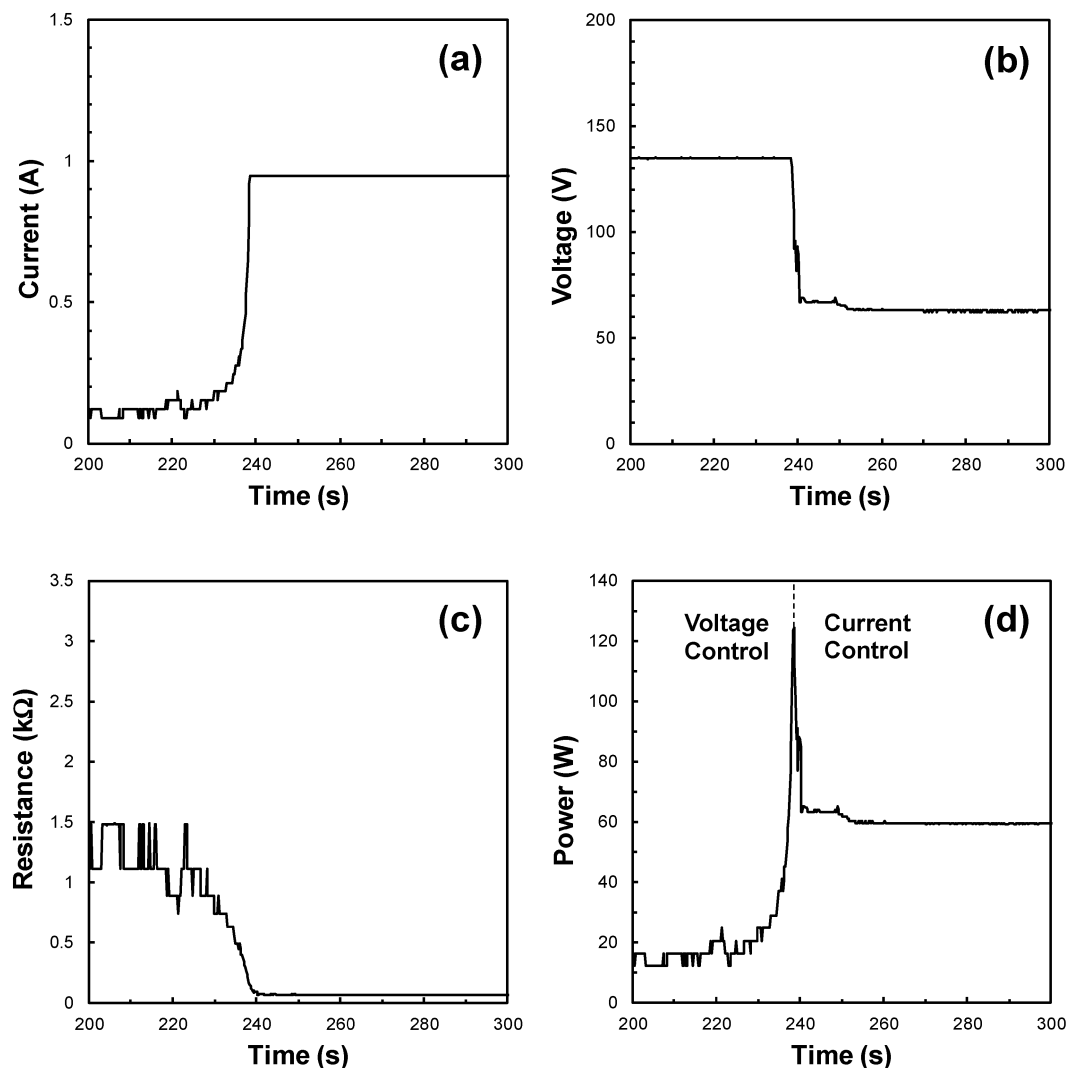


Fig. 2. Current, voltage, resistance and power versus time graphs during flash sintering of 3YSZ under the isothermal condition at 900°C.

In this study, a value of 0.7 was chosen, based on the measurements of Tanaka et al.²⁵⁾ on sintered zirconia. The specimen temperatures calculated from Eq. (3) are given in **Table 1**. The values in Table 1 show a strong effect of the current setting on the specimen temperature during the steady state, rising from 1048 to 1300°C as the current density is increased from 27 to 118 mA/mm².

4.3 Microstructure and densification

Table 1 presents the mean relative density of the central section and average grain size at the center and surface (mid-point of the thickness-length face) of the flash sintered samples. Both the density and the grain size increased with current density, and therefore specimen temperature. Although the mean density reached only 77% at 27 mA/mm² and 1048°C, the sample sintered to a density of 96% with a current of 118 mA/mm² and 1300°C. This is consistent with the results reported in previous literature in which similar densities were obtained with currents of 80–100 mA/mm² with comparable flash sintering durations.^{2),26)} **Figure 4** shows the density as a function of time

around the flash event. The amount of densification before the onset of the flash event was limited. Rapid densification began ~10 s before the switch to current control, but after the onset of the rise in current and power, which began about 20 s before the switch (Fig. 4). The peak densification rate coincided approximately with the switch to current control but densification continued throughout the subsequent 60 s of hold time at constant current, at which point the power supply was switched off.

Figure 3 shows that the specimen, which was initially straight [Fig. 3(a)], developed a pronounced bend around the switch from voltage to current control [Fig. 3(b)]. Subsequently, the specimen slowly straightened again [Fig. 3(c)].

Micrographs of the samples sintered for different limiting current densities are shown in **Fig. 5**. The grain size at the center of the specimen increased with limiting current to a maximum of 238 nm. The grains were significantly smaller at the surface than at the center, and this inhomogeneity was greater with higher current density.

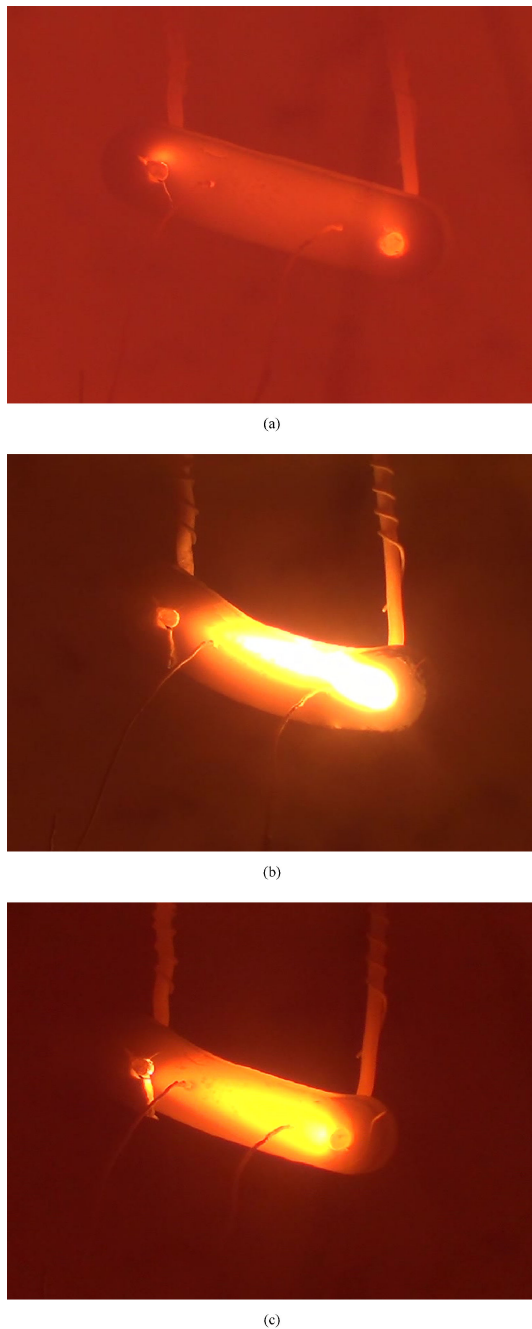


Fig. 3. Stills from videos of the specimen with a current limit of 105 mA. (a) Well before the flash event ($t = 218$ s in Fig. 2), (b) around the flash event ($t = 239$ s in Fig. 2) and (c) well after the flash event ($t = 300$ s in Fig. 2).

4.4 Contact resistance

The apparent contact resistance was calculated using the following equation,

$$R_{\text{contact}} = \frac{1}{I} [V_{\text{pow}} - V_{\text{sam}}(\text{span}_1/\text{span}_2)] - R_{\text{wire}} \quad (4)$$

where R_{contact} is the apparent contact resistance between the Pt electrodes and the sample (Fig. 1), I is the current passing through the sample, V_{pow} is the voltage loaded by the power supply, V_{sam} is the voltage between the inner Pt wires connected to the digital multimeter (Fig. 1), span_1 is

Table 1. Estimated temperature [Eq. (3)], density and average grain size around the center and the surface of the flash sintered samples. The grain sizes for specimens flash sintered under the current densities of 27 and 40 mA/mm² were unmeasurable due to the poorly defined grain boundary of thermally etched samples

Current density mA/mm ²	Estimated Temperature °C	Relative Density %	Grain size	
			Center nm	Surface nm
27	1048	77.0	—	—
40	1119	81.9	—	—
69	1194	91.6	161	113
105	1297	95.8	169	96
118	1300	95.8	238	126

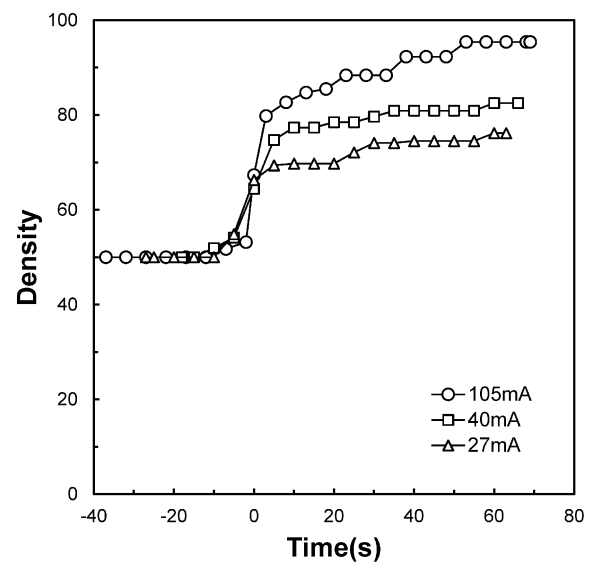


Fig. 4. Density as a function of time around the flash event calculated from dimensions measured from the videos of the sintering specimens. The switch to current control is at time = 0.

the length between the Pt wires connected to the power supply, span_2 is the length between the inner Pt wires connected to the digital multimeter and R_{wire} is the resistance of the Pt wires in the electrical circuit. The equation is based on the assumption of a uniform electric field along the specimen, which allows the potential difference in the specimen between the electrodes to be extrapolated from the potential difference between the inner four-terminal wires.

The ratio of the apparent contact resistance to the apparent specimen resistance, $V_{\text{sam}}(\text{span}_1/\text{span}_2)/I$ is plotted as a function of current in Fig. 6. For the experiment, in the initial voltage control region, the contact resistance was much higher than the specimen resistance but reduced rapidly as the voltage, and therefore the current, increased. This may result from (i) the improved contact between the Pt and the specimen due to local melting/sintering around the contacts, and (ii) decreasing the resistance of the sample near the contact due to local heating. At much higher currents, in the current control regime, the ratio of contact resistance to apparent specimen resistance reduces more gradually, eventually reaching a value of 0.6.

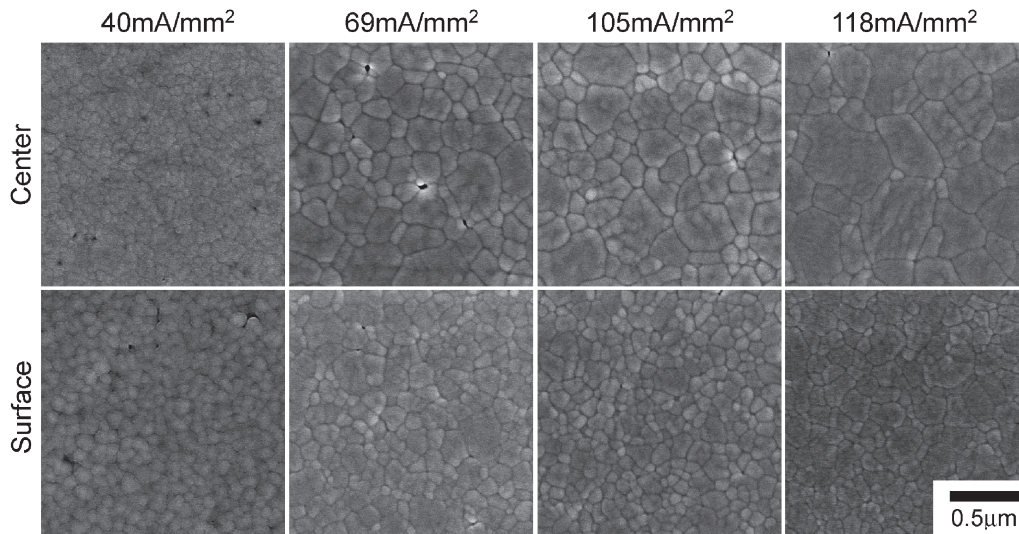


Fig. 5. Microstructure of the sintered samples flashed at 900°C. The photographs were taken around the center and the surface of the samples.

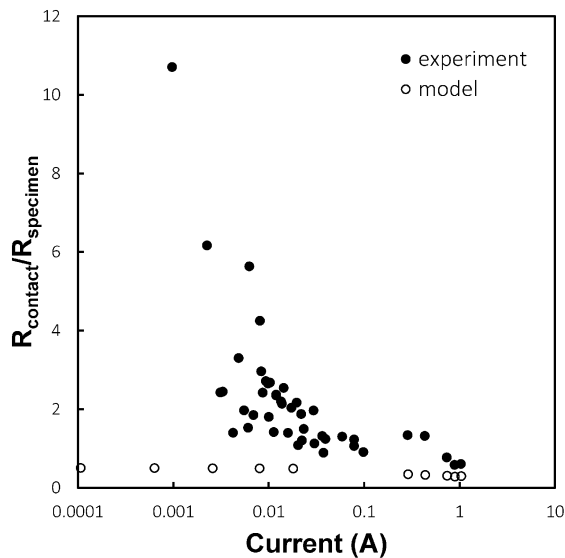


Fig. 6. Experimental and modelled ratio of the apparent contact resistance to the apparent specimen resistance, $V_{\text{sam}}(\text{span}_1/\text{span}_2)/I$, as a function of the current flowing through the specimen.

4.5 Resistivity–temperature relationship

The electrical resistivity ρ was calculated using the 4-terminal method from the following equation:

$$\rho = \frac{V_{\text{sam}}}{I} \frac{A}{L} \quad (5)$$

where I is the measured current, A is the cross-sectional area, and V_{sam} and L are the measured voltage and length between the inner Pt wires, respectively. For the results obtained under voltage control, A and L were assumed to be the same as green body, while for the current control region, in which the shrinkage of the specimen is significant, the dimensions of the sintered bodies were used in the calculation.

Figure 7 shows the results plotted as $\ln \rho$ against $1/T$.

Activation energies Q can be calculated as the gradient of such a plot according to the assumed relationship:

$$\rho = \rho_0 \exp\left(\frac{Q}{RT}\right) \quad (6)$$

which is equivalent to Eq. (1) above. The activation energy for the fully densified sample under low electric field (30 V/cm, negligible Joule heating) was 76 kJ/mol, which is similar to the value of 77 kJ/mol determined previously in the 800 to 1000°C range by Badwal.²¹⁾ It is evident in Fig. 7 that the line of best fit for these results extrapolates well to the results of Kondoh et al.²²⁾ for fully densified 3YSZ at higher temperatures.

The resistivity for the green body under low field (99 V/cm) was initially a factor of ~ 50 greater than that for the dense specimen at the same temperature. The apparent activation energy of the green body exhibited a higher activation energy (~ 126 kJ/mol) than that for the fully densified sample. This was supposed to be the result of the improved particle–particle contacts during heating, resulting in a progressive additional and extrinsic lowering of the resistivity.

The results under constant furnace temperature with higher electrical loading under voltage control and current control are also shown in Fig. 7. When the furnace temperature reached the holding temperature of 900°C, the electric field was increased in a stepwise fashion, and the current passing through the samples increased in response. The temperatures for these results are estimated using the black body model with the same dimensions for the central section of the specimen as for the resistivity. The steep reduction in resistivity of the specimens as the voltage was increased in the voltage control region of Fig. 7 was considered to be a consequence of the continuing particle contact development in the powder compact under the increasing temperature resulting from the Joule heating, which increased the temperature by $\sim 50^\circ\text{C}$ before the flash event was triggered.

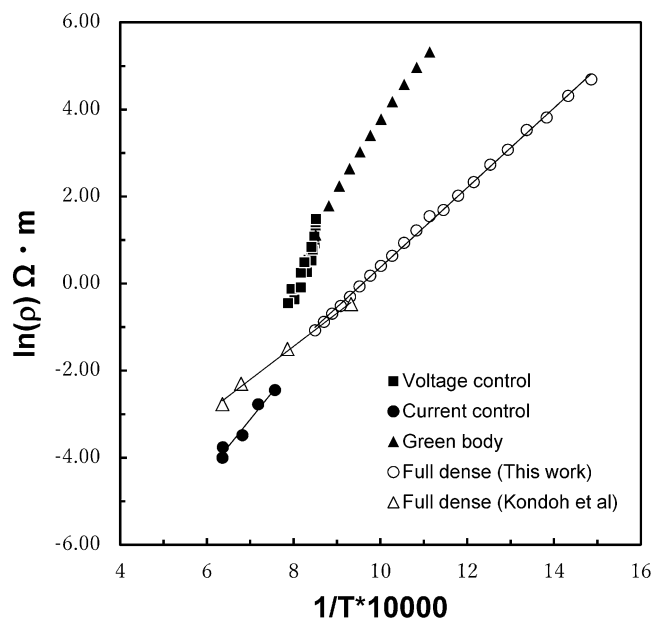


Fig. 7. Inverse Arrhenius plots for resistivity of samples. The temperature refers to the specimen temperature rather than to the furnace temperature.

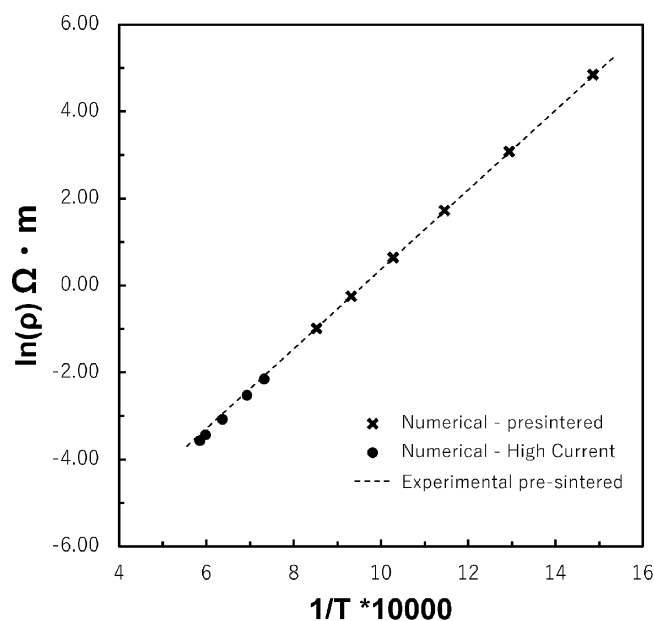


Fig. 8. $\ln \rho$ (Ωm) vs. $1/T(\text{K})$. Line: Eq. (6) using experimental ρ_0 and Q in Table 2 from pre-sintered specimen. X: model of pre-sintered specimen with ρ and specimen temperature T estimated as in the experiments. ● model of high current specimens in constant current region, with ρ and specimen temperature T estimated as in the experiments.

When the “flash event” occurred, triggering the switch to current control, there was a rapid increase in electrical power dissipation, consequent heating and much more extensive shrinkage of the specimen over a few seconds. The resistivity and temperature could not be determined accurately over this period and the current control points on the graph represent the steady state values. The current control resistivity was a factor of ~ 7 lower than that at the end of the voltage control region and lay below the resistivities under conventional heating of Kondoh et al.²²⁾

by a factor of 2–3. The best line of fit to the results from the current control region corresponds to an apparent activation energy Q of 103 kJ mol^{-1} .

5. Modelling

5.1 Resistivity and temperatures using four-terminal tests

Figure 8 shows a plot of $\ln \rho$ against $1/T$ for the model results. The model uses the resistivity temperature relationship of Eq. (6) with the values from the pre-sintered

reference specimen given in **Table 2**. However, temperatures and resistivity in Fig. 8 are calculated from the specimen dimensions, V_{sam} and total current, I , using Eqs (3) and (5) in exactly the same way as for the corresponding experiments. The model correctly returns results corresponding closely to the input resistivity data from the pre-sintered sample, validating the geometry of the 4-terminal test for these specimens.

The model also returns accurate predictions of the underlying resistivity for the high current results, though there is a small shift of the points to the right of the line for the highest currents (i.e. lowest $1/T$) points. This is mainly because the black body Eq. (3) returns the surface temperature, whereas the internal temperatures are higher, as shown in **Table 3**. The black body temperatures calculated from the model results agreed with the average surface temperature between the inner terminals in the model

Table 2. Experimental values of ρ_0 , Q , E_{crit} and ΔT_{crit} compared with predictions from Eqs. (7) and (8) based on resistivity fits in different stages of the process (* = standard deviation)

	Experiment	Constant V	Green body	Pre-sintered
ρ_0 (Ωm)	—	1.29×10^{-10}	5.51×10^{-6}	1.55×10^{-4}
Q (kJ/mol)	—	234	131	76
E_{crit} (V/cm)	$43 \pm 5^*$	44	67	32
ΔT_{crit} (K)	$53 \pm 21^*$	62	139	419

to within 6°C . However, the volume averaged temperature in the model was 45°C higher than the mean surface temperature for the highest current used, and the maximum temperature, near the center of the specimen, was 140°C higher than the surface temperature. Use of the volume averaged temperature shifts the high current points in Fig. 8 back to the input resistivity line (not shown for clarity).

Temperature, current density and electrical power density maps are shown in **Fig. 9**. The maps confirm that the electrical heating is concentrated off-center, along the line between the contact points at the top of the holes, as was found in the experiments. The concentration in power den-

Table 3. Temperatures of the region between the inner terminals extracted from the model. $T_{\text{Avg Sur}}$ and $T_{\text{Avg Vol}}$ are the average surface and volume temperatures in this region and T_{Max} is the maximum temperature. T_{BBM} is the temperature calculated using the black body model exactly as in the experiments, i.e. using Eq. (3)

Current density mA/mm^2	$T_{\text{Avg Sur}}$ $^\circ\text{C}$	$T_{\text{Avg Vol}}$ $^\circ\text{C}$	$T_{\text{Max Vol}}$ $^\circ\text{C}$	T_{BBM} $^\circ\text{C}$
27	1098	1110	1139	1092
40	1174	1192	1207	1170
69	1301	1333	1389	1297
105	1401	1440	1510	1399
118	1440	1485	1580	1436

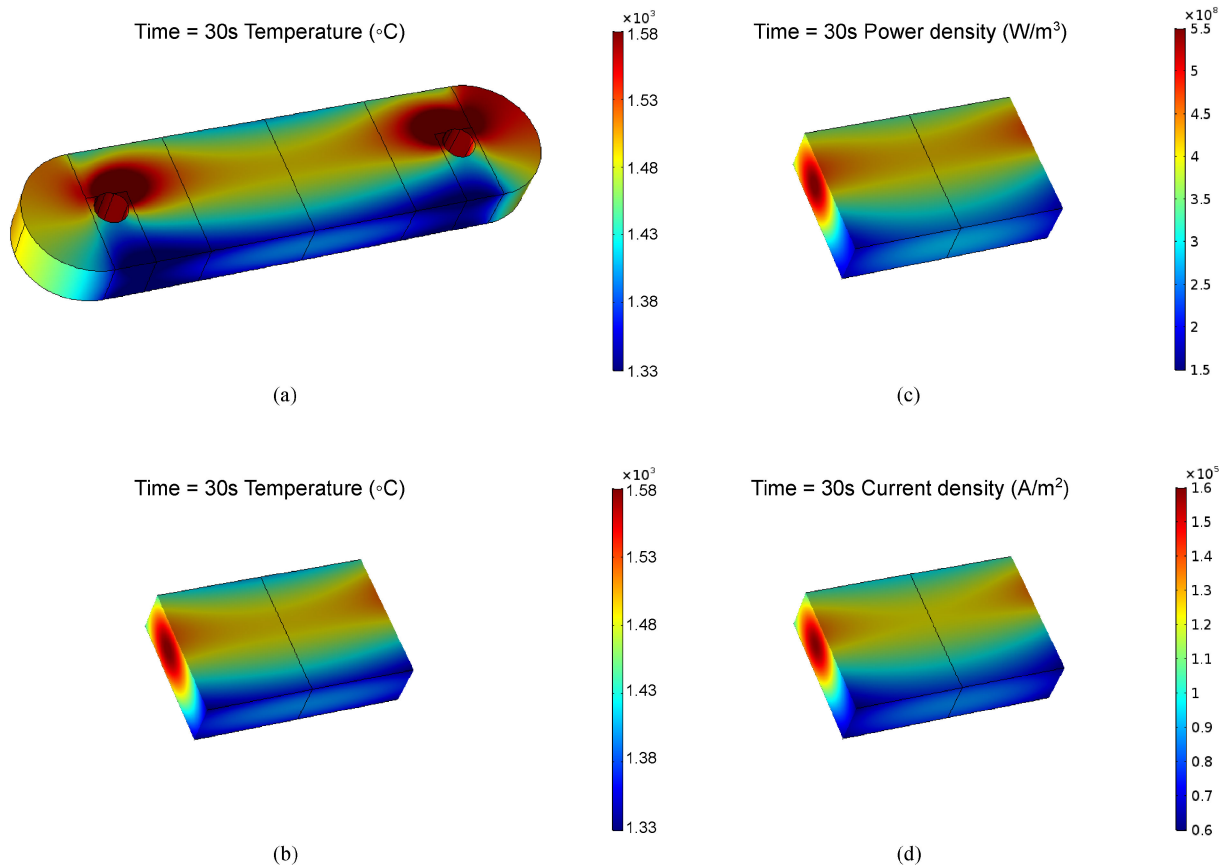


Fig. 9. Model distributions predicted by the model for the $118 \text{ mA}/\text{mm}^2$ high current specimen. (a) Temperature, whole specimen, (b) temperature, central section between inner terminals, (c) power density, (d) current density.

sity shows that the temperature is higher in the specimen interior not only because a temperature gradient is necessary to drive the heat generated to the surface but also because the higher temperature reduces the resistivity in the interior.

Given the highly non-uniform temperature and current density in Fig. 9, it is surprising that the analysis method used in the experiments, which assumes uniform temperature and uniform current density [implicit in Eqs. (3) and (5)], yields resistivity values which agree so closely with the underlying resistivity rule in Fig. 8. This may be coincidental to some extent in that the higher temperature and current density in the specimen center than the simple analysis assumes are offset by the smaller cross-sectional area of this concentrated region; this analysis method may be less accurate with different specimen sizes, shapes or current limits. The use of modelling as used here to establish the details of temperature and current flow is recommended to ensure valid measurements.

5.2 Contact resistances

The basic model includes no real contact resistance but apparent contact resistances arose when calculated according to Eq. (4) because the electrical geometry does not conform to the uniform electric field assumption implicit in the equation. Instead, the current is forced to converge towards the small point of contact between the electrode and the specimen. The apparent contact resistances in the model, calculated according to Eq. (4) are shown in Fig. 6. At low current (and therefore low temperature) the apparent contact resistance in the model is an order of magnitude smaller than the experimental value demonstrating that a substantial, physical contact resistance is present in the low temperature experiments. In the high current (high temperature) results, the apparent contact resistance in the model is about 0.3 of the specimen resistance, which is about half the experimental value, so although there is a geometrical effect, a physical contact resistance remains.

Use of the 2 terminal data from the model (i.e. the power dissipated between the electrodes and the full surface area of the specimen between them) in the black body model for temperature estimates rather than the 4 terminal results increased the black body estimation of temperature by 92°C for the highest constant current used (118 mA/mm²), even without the inclusion of any physical contact resistance. The black body model should therefore be treated with caution for 2-terminal data.

6. Discussion

6.1 Effect of sintering on resistivity

The resistivity-temperature relationship from the low voltage, pre-sintered specimens shown in Fig. 7 is consistent with previous reports^{21),22)} and provides a useful baseline for comparison with the flash sintering results. These are evidently very different and fall into three sections. Starting with the green body, the initial resistivity is much higher than that of the pre-sintered specimen because of the large amount of porosity and poor contact at

particle-particle boundaries. Previous work has shown that with constant porosity, the activation energy is unaffected by the pores,^{27),28)} but here, as the specimen heats, the resistivity vs. 1/T plot always has a steeper gradient than that of the pre-sintered reference specimens. This is attributed to the continual improvement of the particle-particle contacts and therefore reduction in resistivity as heating takes place. The effect accelerates, leading to a constant downward curvature of the $\ln \rho$ against 1/T plots as temperature increases (i.e. 1/T decreases) and a higher apparent activation energy.

When the voltage is applied and stepped up, the slope of the $\ln \rho$ vs. 1/T plot continues to increase further. Recent in situ observations of the sintering of the same powder show that sintering begins above ~900°C in the absence of an electric field and the onset temperature, at which 1% densification has taken place, is 960°C.²⁹⁾ The mean estimated temperature just before the “flash event” for the present specimens was 968°C, so it is clear that although the amount of shrinkage is small at this stage, as is confirmed by the video measurements such as Fig. 3(a), grain boundary formation at particle contacts, neck growth and the reduction of porosity through conventional sintering are all expected to occur at this point on the grounds of the temperature alone, although an additional, direct effect of the electric field or current cannot be ruled out completely by such a qualitative analysis.

6.2 Influence of sintering on the onset of flash sintering

The relationship between furnace temperature and electric field for the onset of flash sintering in 3YSZ has recently been predicted successfully on the basis of thermal runaway.¹⁴⁾ The resistivity-temperature relationship was described phenomenologically in Ref. 14) by an inverse Arrhenius expression, as in the present paper and was fitted to results from flash sintering green bodies. However, the activation energy of 171 kJ/mol was much higher than the accepted high temperature value for 3YSZ of 60–80 kJ/mol. The more detailed results in Fig. 7 show the reason for this is the reduction of resistivity by the early stages of sintering as discussed in the previous section.

A simple analytical expression was derived in Ref. 14) for the critical electric field, E_{crit} , at which a rod of circular cross section would first undergo thermal runaway with a furnace temperature T_0 when radiative heat loss dominates. The equivalent derivation for a bar of arbitrary cross-section gives:

$$E_{\text{crit}}^2 = \frac{4P\varepsilon\sigma\rho_0 R}{AQ} (T_0 + \Delta T_{\text{crit}})^5 \exp\left[\frac{Q}{R(T_0 + \Delta T_{\text{crit}})}\right] \quad (7)$$

in which for $\Delta T_{\text{crit}} \ll T_0$:

$$\Delta T_{\text{crit}} \approx \frac{RT_0^2}{Q - 5RT_0} \quad (8)$$

where P and A are the perimeter and area respectively

of the specimen cross section, ρ_0 and Q are the pre-exponential and activation energy in Eq. (6), R is the gas constant, ε is the emissivity, σ is Stefan's constant and ΔT_{crit} is the amount by which the specimen exceeds the furnace temperature at runaway.

Using the best fit straight line to the constant voltage results in Fig. 7, which immediately precede the flash event, the prediction of Eqs. (7) and (8) is shown in Table 2. Table 2 also shows the experimental results and the values of E_{crit} and ΔT_{crit} predicted from the inverse Arrhenius fits to the results in Fig. 7 for the green body and the pre-sintered control specimen. The comparison shows that Eqs. (7) and (8) correctly predict the conditions for the flash event to within experimental error when the electrical characteristics in the constant voltage region in which the event occurs are used, but that the use of the characteristics extrapolated from other conditions predicts higher electric fields than are observed experimentally. We conclude that the pre-flash sintering influences the onset criterion under the present conditions and must be taken into account. A more detailed treatment should consider the effect of sintering with time as well as temperature.

Raj has recently presented an analysis of experimental results claiming to show that the flash event occurs under subcritical conditions according to the energy balance approach underpinning Eq. (7).³⁰⁾ However, the analysis in Ref. 30) uses the activation energy measured at low temperature, in the green body regime, rather than using the electrical properties in the conditions under which the flash event actually occurs. The present results and analysis show that this approach is flawed because it does not account for the change in activation energy due to the early stages of sintering; when this is accounted for, by using the electrical properties in the regime of relevance, the present work shows that Eq. (7) correctly predicts the onset criterion for flash sintering based on thermal runaway. Interestingly, Ref. 30) tends to show less discrepancy on high field/low critical temperature results. This is expected because the extrapolation from low temperature results is less extreme and initial sintering has less effect. There are now several independent reports on a range of different materials concluding that the flash event corresponds well to thermal runaway.^{14)–18)}

6.3 Resistivity at high currents

After the flash event, the specimens were much denser (Table 1) and this, along with the much higher specimen temperature from Joule heating accounts for much of the further reduction of resistivity shown by the results under current control in Fig. 7. However, the extent of this reduction is such that the constant current specimens all showed a lower resistivity for a given temperature than the extrapolation of the base-line, pre-sintered results or the results of Kondoh et al.,²²⁾ even though some have a density as low as 77%. Although the underestimate of the temperature by the blackbody Eq. (3) contributes to this, the model results in Fig. 8 show that this factor is too small to explain the discrepancy in Fig. 7.

Another possibility is that the contact resistance produces excess heat at the electrodes which is then conducted into the central part of the specimen, so that the true temperature of the central part is higher than is calculated by Eq. (3), which assumes that no heat flows along the length of the specimen. This was investigated by artificially inserting resistive elements at the electrodes in the model to match the measured contact resistances. This did move the model results toward the experimental points (not shown) but by much less than would be required to match them.

This leaves the possibility that the results are correct and the resistivity of the YSZ is lowered under high DC current. There is other evidence that this may be the case. Under the low voltage conditions of the pre-sintered specimen, ionic conduction is considered to be the dominant mechanism. However, Maso and West³¹⁾ have recently shown reductions in resistance of 8YSZ under DC bias, though at lower temperatures than those used here. The observations were attributed to a significant component of electronic conduction as a result of the DC electric field. Earlier work by Janek and Korte³²⁾ on the blackening of YSZ single crystals at the cathode under electrochemical reduction also concluded that the reduction led to a higher electronic conductivity than in the ionic conductivity of unreduced material. Darkening of YSZ due to reduction under flash sintering conditions has recently been observed by Morisaki et al.³³⁾ Darkening of the specimens near the cathode was also observed here and is not surprising given the difficulty of reducing sufficient atmospheric oxygen to maintain ionic conduction at the small contact area between the Pt electrode and the specimen in our specimens. This provides a plausible explanation for the low resistivity of the constant current specimens in Fig. 7 and is also consistent with the slightly higher experimental apparent activation energy evident in the constant current regime. Dong et al.³⁴⁾ have also recently discussed the possibility of lowered resistivity as a result of electronic conduction caused by reduction of YSZ under flash sintering conditions.

The reduction in resistivity from this reduction seems to be smaller than the effect of sintering but should also be taken into account for accurate prediction of the flash conditions.

This may also be relevant to the asymmetry of the light emissions observed in Figs. 3(b) and 3(c), in which the specimen is brighter near the anode. Whether this is an asymmetry in heating or in the electroluminescence which has been reported in Ref. 35) is not clear and further investigation is needed. Note that the present investigation only involves results from a short section of the gauge length so the assumption of uniform conditions between the inner four terminal wires should not lead to significant errors.

6.4 Densification and grain growth

The densification and grain growth correlate with temperature: the density increases with temperature in the

constant current regime and the grain size is greater in the center of the specimen than at the edge, where the temperature is lower. Of course, the same correlations can be made with current or electrical power dissipation, through the higher current limit responsible for the higher temperature in the former case and through the localisation of current and power dissipation shown in Figs. 9(c) and 9(d) for the latter. However, it is clear that the electric field itself is not responsible for enhanced densification: comparison of Figs. 2 and 4 show that densification is slow in the constant voltage regime until the current, and therefore the electrical power responsible for Joule heating, increases at the onset of the flash event; in addition, most of the densification occurs in the constant current regime, where the electric field is decreasing.

Table 1 shows that the specimens reach 92% density with a specimen temperature of 1194°C and 96% with a specimen temperature of 1300°C, both with hold times of 1 min. The modelling suggests that these black body values are lower bounds for the volume averaged temperatures. We have recently shown that the same slip cast powder compacts can be sintered to 99% density in ~30 s by rapid heating to 1300°C without applying an electric field or current to the specimen.²⁰⁾ The confirmation here that similar temperatures are required to reach high sintered density on the same timescale when some of the specimen heating is electrical in origin supports the idea that rapid heating rather than the application of an electric field is the most important factor in accelerating densification in flash sintering.

6.5 Bending of specimens during flash sintering

The off-center temperature maximum in experiment [Fig. 3(b)] was successfully reproduced in the model [Fig. 9(b)] and is a consequence of the electrodes making contact at the top side of the holes in the specimen because of the suspension method shown in Fig. 1. This provides a ready explanation for the shape change of the specimens during flash sintering. The top half of the specimen initially sinters faster than the bottom half because it is hotter and the resulting asymmetric shrinkage leads to the bending seen in Fig. 3(b). Subsequent sintering of the lower half of the specimen then causes the specimen to straighten as seen in Fig. 3(c).

7. Conclusions

In this study, we evaluated electrical resistivity during the flash sintering of 3YSZ by the four-terminal method accompanied by numerical modelling. The conclusions obtained are summarized as follows.

(1) The contact resistance was sensitive to changes in the current. Without the aid of conductive paint, the observed contact resistance decreased by three orders of magnitude during the flash sintering, but remained significant even for high currents.

(2) The resistivity in the central part of the specimens described here could be estimated accurately between the

inner 4 point terminals. However, contact resistance (in 2 terminal measurements), specimen geometry and temperature localization all have the potential to cause significant errors in resistivity measurements under other conditions.

(3) Black body temperature estimates under high current conditions reflect the surface temperature at best and severe errors of 100°C or more result from temperature gradients, contact resistances (for two terminal measurements) and geometrical non-uniformities such as point contacts. Despite this, the modelling suggests that surface temperatures could be estimated accurately between the inner 4 point terminals.

(4) High electrical currents cause a reduction of the resistivity for a given specimen temperature compared with low current measurements in which ionic conductivity is dominant. This was attributed to electronic conduction associated with reduction of the YSZ.

(5) The onset of flash sintering is accurately predicted on the basis of thermal runaway but only if the electrical properties under the relevant conditions are used. In particular, the early stages of sintering gradually reduce the resistivity and affect the apparent activation energy under the conditions used here. This effect of sintering on electrical properties, along with any early effect of reduction, must be taken into account for the onset of flash sintering to be predicted correctly.

(6) The sintering rates under flash sintering of 3YSZ were similar to those in similar specimens subjected to rapid heating to the same temperature without the use of electricity. Density and grain growth both correlated with local specimen temperature. Differential sintering caused by temperature gradients and non-uniform electrical heating led to specimen distortion.

Acknowledgements We are grateful to Dr. E. Zapata-Solvas of Imperial College London for his significant contribution of assembling the furnace for flash sintering. We would like to thank to Dr. R. S. Bonilla of University of Oxford for his helpful discussions.

References

- 1) M. Cologna, B. Rashkova and R. Raj, *J. Am. Ceram. Soc.*, **93**, 3556–3559 (2010).
- 2) M. Cologna, A. L. G. Prette and R. Raj, *J. Am. Ceram. Soc.*, **94**, 316–319 (2011).
- 3) A. L. G. Prette, M. Cologna, V. Sglavo and R. Raj, *J. Power Sources*, **196**, 2061–2065 (2011).
- 4) A. Gaur and V. M. Sglavo, *J. Eur. Ceram. Soc.*, **34**, 2391–2400 (2014).
- 5) A. Gaur and V. M. Sglavo, *J. Mater. Sci.*, **49**, 6321–6332 (2014).
- 6) A. Karakuscu, M. Cologna, D. Yarotski, J. Won and J. S. C. Francis, *J. Am. Ceram. Soc.*, **95**, 2531–2536 (2012).
- 7) M. Cologna, J. S. C. Francis and R. Raj, *J. Eur. Ceram. Soc.*, **31**, 2827–2837 (2011).
- 8) R. Muccillo and E. N. S. Muccillo, *J. Eur. Ceram. Soc.*, **34**, 915–923 (2014).
- 9) E. Zapata-Solvas, S. Bonilla, P. R. Wilshaw and R. I. Todd, *J. Eur. Ceram. Soc.*, **33**, 2811–2816 (2013).

- 10) V. M. Candelario, R. Moreno, R. I. Todd and A. L. Ortiz, *J. Eur. Ceram. Soc.*, **37**, 485–498 (2017).
- 11) H. Yoshida, Y. Sakka, T. Yamamoto, J.-M. Lebrun and R. Raj, *J. Eur. Ceram. Soc.*, **34**, 991–1000 (2014).
- 12) R. Raj, M. Cologna and J. S. C. Francis, *J. Am. Ceram. Soc.*, **94**, 1941–1965 (2011).
- 13) K. S. Naik, V. M. Sglavo and R. Raj, *J. Eur. Ceram. Soc.*, **34**, 4063–4067 (2014).
- 14) R. I. Todd, E. Zapata-Solvas, R. S. Bonilla, T. Sneddon and P. R. Wilshaw, *J. Eur. Ceram. Soc.*, **35**, 1865–1877 (2015).
- 15) Y. Y. Zhang, J. I. Jung and J. Luo, *Acta. Mater.*, **94**, 87–100 (2015).
- 16) E. Bichaud, J. M. Chaix, C. Carry, M. Kleitz and M. C. Steil, *J. Eur. Ceram. Soc.*, **35**, 2587–2592 (2015).
- 17) J. G. P. da Silva, H. A. Al-Qureshi, F. Keil and R. Janssen, *J. Eur. Ceram. Soc.*, **36**, 1261–1267 (2016).
- 18) M. Biesuz and V. M. Sglavo, *J. Eur. Ceram. Soc.*, **36**, 2535–2542 (2016).
- 19) Y. Zhang, J. Nie, J. M. Chan and J. Luo, *Acta. Mater.*, **125**, 465–475 (2017).
- 20) W. Ji, B. Parker, S. Falco, J. Y. Zhang, Z. Y. Fu and R. I. Todd, *J. Eur. Ceram. Soc.*, **37**, 2547–2551 (2017).
- 21) S. P. S. Badwal, F. T. Ciacchi and R. H. J. Hannink, *Solid State Ionics*, **40–41**, 882–885 (1990).
- 22) J. Kondoh, T. Kawashima, S. Kikuchi, Y. Tomii and Y. Ito, *J. Electrochem. Soc.*, **145**, 1527–1536 (1998).
- 23) R. Raj, *J. Eur. Ceram. Soc.*, **32**, 2293–2301 (2012).
- 24) COMSOL Multiphysics® v. 5.2. www.comsol.com. COMSOL AB, Stockholm, Sweden.
- 25) H. Tanaka, S. Sawai, K. Morimoto and K. Hisano, *J. Therm. Anal. Calorim.*, **64**, 867–872 (2001).
- 26) J. S. C. Francis and R. Raj, *J. Am. Ceram. Soc.*, **96**, 2754–2758 (2013).
- 27) Y. Du, A. J. Stevenson, D. Vernat, M. Diaz and D. Marinha, *J. Eur. Ceram.*, **36**, 749–759 (2016).
- 28) M. C. Steil, F. Thevenot and M. Kleitz, *J. Electrochem. Soc.*, **144**, 390–398 (1997).
- 29) H. Majidi, T. B. Holland and K. van Benthem, *Ultramicroscopy*, **152**, 35–43 (2015).
- 30) R. Raj, *J. Am. Ceram. Soc.*, **99**, 3226–3232 (2016).
- 31) N. Masó and A. R. West, *Chem. Mater.*, **27**, 1552–1558 (2015).
- 32) J. Janek and C. Korte, *Solid State Ionics*, **116**, 181–195 (1999).
- 33) N. Morisaki, H. Yoshida, K. Matsui, T. Tokunaga, K. Sasaki and T. Yamamoto, *Appl. Phys. Lett.*, **109**, 083104 (2016).
- 34) Y. Dong, H. Wang and I.-W. Chen, *J. Am. Ceram. Soc.*, **100**, 876–886 (2017).
- 35) K. Terauds, J.-M. Lebrun, H.-H. Lee, T.-Y. Jeon, S.-H. Lee, J. H. Je and R. Raj, *J. Eur. Ceram. Soc.*, **35**, 3195–3199 (2015).